Benchmarking promoters of Fe/activated carbon catalyst for stable hydrogenation of CO_2 to liquid hydrocarbons

Jingyu Chen [a,b], Seung Ju Han [b], Hae-Gu Park [b], Khasan Nasriddinov [a,b], Chundong Zhang [c], Ki-Won Jun [a,b,*], Seok Ki Kim [d,e,**]

[a] Advanced Materials and Chemical Engineering, University of Science and Technology (UST), Daejeon 34114, Republic of Korea
[b] C1 Gas Conversion Research Group, Carbon Resources Institute, Korea Research Institute of Chemical Technology (KRICT), Daejeon 34114, Republic of Korea
[c] State Key Laboratory of Materials-Oriented Chemical Engineering, College of Chemical Engineering, Nanjing Tech University, Nanjing 211816, China
[d] Department of Energy Systems Research, Ajou University, Suwon 16499, Republic of Korea
[e] Department of Chemical Engineering, Ajou University, Suwon 16499, Republic of Korea

ARTICLE INFO

ABSTRACT

Although iron-based catalysts are effective for long-chain hydrocarbon formation during the hydrogenation of CO_2, they easily undergo deactivation. Thus, the deactivation behaviors of Fe-based catalysts supported on active carbon were investigated using various promoters. Ten metals were selected as promoters, and the resulting catalytic activities and selectivities over the course of 100 h were evaluated. Catalyst deactivation was primarily caused by changes of active phase and active crystallite size, namely active site transitions. Although the oxidation of Fe carbide is an unavoidable process, this can be alleviated by increasing the crystallite size to expose greater numbers of active sites and compensate for the deactivation process. The Cu-modified catalyst exhibited the highest CO_2 conversion and C_{5+} yield, but was easily deactivated. In contrast, the Zn-modified catalyst exhibited stable activity, good C_{5+} yield, and high olefin/paraffin ratio by inhibiting oxidation and exhibiting a large increase in the active crystallite.

1. Introduction

Anthropogenic CO_2 emissions from fossil fuel combustion and other human activities disrupt the natural environment, resulting in global warming and ocean acidification. Carbon capture and utilization (CCU) technologies have therefore received growing interest as an efficient means to convert CO_2 and lower environmental CO_2 concentrations [1, 2]. To date, numerous studies have focused on using CO_2 as a material for producing value-added chemicals, such as methanol, methane, olefins, and liquid fuels [3–6]. In addition, with the assistance of green hydrogen (H_2) derived from renewable energy-powered water electrolysis, the concept of power-to-liquid (PTL) can offer a means to realize a potentially carbon-neutral fuel cycle and the sustainable production of synthetic fuels [6,7]. For example, the extraction of CO_2 from air and its combination with H_2 under specific conditions can produce hydrocarbons. This process appears to be a closed cycle in which the products, following their combustion and release into the atmosphere as CO_2, continue to react with H_2, resulting in zero net CO_2 emissions [8,9].

It is widely known that liquid hydrocarbon (C_{5+}) fuels have a larger market for use as transportation fuels and value-added chemicals [10, 11]. Consequently, the conversion of CO_2 into C_{5+} hydrocarbons has proven to be a promising method for CO_2 utilization. Generally, this is achieved obtained by reducing CO_2 to CO via the reverse water gas shift (RWGS) reaction and then reacting CO with additional hydrogen via the classical Fischer-Tropsch synthesis (FTS) route [12,13]. Among the group VIII metals that are candidates for the FTS process, Fe-based

catalysts possess high catalytic activities in both the RWGS and FTS reactions due to the fact that they contain multiphase active sites, including Fe oxides and Fe carbides [14,15].

The catalytic stability is a crucial characteristic for the practical application of Fe-based catalysts. This is because the activities of Fe-based catalysts decrease during the FTS reaction owing to high deactivation rates, which can be attributed to metal particle sintering, carbon deposition, and phase transformation, for example [14,16,17]. The primary cause of deactivation for the different catalysts available for the CO_2-FTS remains is a hotly debated topic, with a number of deactivation mechanisms being described in the literature [18–21]. More specifically, it has been proposed that the active iron carbide phases gradually transform into fewer active or inactive phases, which are then oxidized or interconverted into different types of iron carbide species. In addition, it has been suggested that the catalyst surface suffers from the deposition of inactive carbonaceous compounds, including graphitic carbon, amorphous carbon, and coke. These materials hinder the contact between the reactant gases and the active sites of the catalysts, thereby impeding product formation. Furthermore, the sintering of active phases has been considered to play a role in catalyst deactivation due to its association with a reduction in the surface area through ripening, migration, or coalescence of the iron phase. Consequently, the deactivation of Fe-based catalysts has received growing attention to obtain further insight into their structures and to develop approaches to extend their lifetimes [15,19,22]. In this context, Hong et al. investigated the possibility that the deactivation behavior of a co-precipitated Fe-Cu-K-Al catalyst could be caused by an increase in the crystallinity of the iron species, resulting in partial component separation [16]. Additionally, Hwang et al. predicted that the deactivation pathway of Fe–K/γ-Al$_2$O$_3$ catalysts is highly susceptible to secondary reactions at the reactor outlet due to carbon deposits [23]. In addition, Zhang et al. proposed that the predominant deactivation behavior of the pure iron catalyst results from the phase transformation of the iron phase (Fe$_5$C$_2$ → Fe$_3$O$_4$) throughout its lifetime [15].

Thus, to enhance the catalytic activity and stability of Fe systems, the addition of metal promoters is commonly employed, such as alkali promoters (e.g., K, Na), alkaline earth promoters (e.g., Ca, Mg), or transition metals (e.g., Mn, Cu, Zn), which accelerate the conversion of CO_2 and the carbonization of iron. For example, Zhang et al. reported that introducing Zn into an Fe catalyst inhibited the oxidation of FeC$_x$, thereby stabilizing the catalyst and slowing deactivation [14]. In addition, Wang et al. reported that Ni as a promoter in the Na-mediated bimetallic Fe–Ni catalysts could regulate iron carbide formation and overcome carbon deposition due to the reduced adsorption and dissociation of CO on Ni metal, ultimately resulting in a relatively stable CO hydrogenation reaction activity [24]. Furthermore, Bashiri et al. studied the FeCo-LaK catalyst for CO_2 hydrogenation and discovered that the addition of La as a promoter deactivated the catalyst owing to the strong acidic sites on La promoting carbon deposition [25]. For the activated-carbon-supported catalyst, Ma et al. reported that the addition of Mo to the Fe-Cu-K/AC catalyst effectively retarded the deactivation rate in the FTS process by preventing agglomeration of iron active sites during the reaction [26]. These previous studies therefore highlight the importance of introducing a promoter to maintain high activity levels and prevent catalyst deactivation; however, the promoter must be carefully selected to prevent catalyst deactivation.

Thus, we herein report our investigation of thirteen different promoters, including alkali, alkaline earth, transition metal, lanthanide, and group III metal promoters, for use in the CO_2-FTS reaction over an Fe-based catalyst supported by an activated carbon material. In addition, to interpret the deactivation mechanism, analyses by X-ray diffraction (XRD), nitrogen (N_2) adsorption–desorption isotherms, Raman spectroscopy, and differential scanning calorimetry–thermogravimetric analysis (DSC-TG) are carried out. Ultimately, we aim to provide an essential concept for extending the catalyst activity and selecting promoters to achieve an optimal catalyst stability and selectivity.

2. Experimental

2.1. Materials

Activated carbon (AC) was supplied by Samchully Activated Carbon Company as the raw material. The specific surface area and pore volume of the AC were 920 m^2/g, 0.39 cm^3/g, respectively. Iron(III) nitrate [Fe(NO$_3$)$_3$•9H$_2$O, 98.5%], copper(II) nitrate [Cu(NO$_3$)$_2$•3H$_2$O, 99%], potassium carbonate (K$_2$CO$_3$, 99.5%), anhydrous ethanol (99.9%), cobalt (II) nitrate hexahydrate [Co(NO$_3$)$_2$•6H$_2$O, 97%], calcium nitrate tetrahydrate [Ca(NO$_3$)$_2$•6H$_2$O, 98.5%], zinc nitrate hexahydrate [Zn(NO$_3$)$_2$•6H$_2$O, 98%], and nickel(II) nitrate hexahydrate [Ni(NO$_3$)$_2$•6H$_2$O, 98%] were purchased from Samchun Chemicals (Seoul). Indium nitrate (InN$_3$O$_9$, 99.5%), ammonium (para) tungstate hydrate (H$_{42}$N$_{10}$O$_{42}$W$_{12}$•xH$_2$O, 99%), gallium(III) nitrate hydrate (GaN$_3$O$_9$•xH$_2$O, 99.9%), cerium(III) nitrate hexahydrate [Ce(NO$_3$)$_3$•6H$_2$O, 99%], and barium nitrate (BaN$_2$O$_6$, 99%) were purchased from Sigma Aldrich. Manganese(II) nitrate hexahydrate [Mn(NO$_3$)$_2$•3H$_2$O, 97%] and boric acid (H$_3$BO$_3$, 99.5%) were obtained from Junsei Chemical Co., Ltd. All chemicals were used as received without further purification.

2.2. Catalyst preparation

Preparation of the Fe/AC catalyst: The Fe precursor was dispersed on AC using the ultrasonic-assisted melt-infiltration method to create the Fe/AC catalyst. More specifically, Fe(NO$_3$)$_3$•9H$_2$O (1.85 g) was dissolved in ethanol (20 mL), and AC (1 g) was then added as a support. The resulting mixture was subjected to ultrasonic irradiation for 4 h to obtain a clear solution. After this time, the sample was dried overnight at 80 °C to remove the ethanol, and the solid sample was calcined under N_2 at 450 °C for 5 h.

Preparation of the KFe/AC catalyst: The potassium-promoted catalyst (KFe/AC) was synthesized using the incipient wetness impregnation (IWI) technique. For this purpose, the desired quantity of potassium (K/Fe weight ratio = 0.25) was loaded onto the Fe/AC catalyst using potassium carbonate (K$_2$CO$_3$) as the source material. After thorough impregnation and dispersion, the KFe/AC specimen was dried at 120 °C for 12 h in an oven and calcined under N_2 at 500 °C for 5 h.

Preparation of the M-KFe/AC catalysts: A second metal (M = Cu, Co, Ce, Zn, Mn, In, Ga, W, B, Ni, Ca, and Ba) was added into KFe/AC catalyst as a promoter using the same IWI technique with a M/Fe weight ratio of 0.13. After thorough impregnation and dispersion, the obtained specimen was dried at 120 °C for 12 h and calcined under N_2 at 450 °C for 5 h.

2.3. Characterization

The XRD spectra were acquired using a Rigaku Ultima IV diffractometer with Cu Kα (λ = 1.5406 Å) radiation at 40 kV and 40 mA. The patterns were recorded in the range of 10–90° [scanning angle (2θ)] with a step size of 0.02°. The crystallite size was estimated using the Scherrer equation:

$$D = \frac{0.89\lambda}{\Delta\cos\theta}$$

where D refers to the crystal size, $λ$, $Δ$, and $θ$ are the wavelength of the X-rays, the full width at half maximum (FWHM) of the diffraction peak, and the angle correlated to the peak, respectively. The crystallite sizes of the fresh, activated, and used catalysts corresponded to the characteristic (311) facet of Fe$_3$O$_4$ and the (510) facet of Fe$_5$C$_2$. Additionally, the phase compositions and contents of all samples were analyzed by Rietveld refinement of the XRD patterns.

The surface area and pore structure of each specimen were determined by means of N_2 adsorption–desorption measurements at $-196\,°C$ using an ASAP-2400 analyzer (Micromeritics). Prior to carrying out the measurements, the samples were degassed at $90\,°C$ for 30 min and heated at $150\,°C$ for 4 h under vacuum. The Barrett–Joyner–Halenda (BJH) method was used to determine the pore structure, whereas the Brunauer–Emmett–Teller (BET) method was used to analyze the surface area. Raman spectra were collected using a Raman spectrometer (HORIBA, LabRAM HR Evolution) and an argon-ion laser (Ar^+, 514.5 nm) under ambient conditions. Additionally, thermal DSC-TG analyses were performed using an SDT Q600 thermogravimetric analyzer and a differential scanning calorimeter. For this purpose, each sample (~20–30 mg) was heated from $30°$ to $900°C$ at a rate of $10\,°C/$ min under a 100 mL/min airflow. The resulting curves were used to determine the decomposition of the carbon species.

X-ray photoelectron spectroscopy (XPS) was performed to analyze chemical and electronic states by Kratos Axis Supra spectrometer. An incident monochromated Al Kα line was used for sample excitation and the binding energy (BE) was calibrated using the C 1 s peak at 284.8 eV. CO_2 temperature -programmed desorption (CO_2-TPD) was conducted to analyze the surface basicity using a Micromeritics Autochem 2920 apparatus. The samples (50 mg) were pretreated in a flow of 10% H_2/Ar (30 mL/min) at $400\,℃$ for 1 h and then cooled to $50\,℃$ under He. After 10% CO_2/He uptake at $50\,℃$ for 1 h, the CO_2 desorption was conducted from $50\,℃$ to $800\,℃$ in a He flow 50 mL/min. The high-resolution transmission electron microscopy (HR-TEM, Talos F200S) was carried out to observe the crystal lattice fringe information with an accelerating voltage of 200 kV. The high-angle annular dark-field-scanning

transmission electron microscopy (HAADF-STEM) images and energy-dispersive X-ray spectroscopy (EDS) mapping was used to observe elemental distribution.

2.4. Reaction test

The CO_2 hydrogenation reaction was conducted in a stainless steel fixed-bed reactor measuring 350 mm in length, and with an inner diameter of 7.35 mm. Each reaction was conducted using 0.3 g of the catalyst (Fe/AC, KFe/AC, or M-KFe/AC), which was mixed with ɣ-Al_2O_3 as a diluent (1.5 g) and loaded into the center of the reactor. Prior to evaluation, the sample was reduced in situ with syngas (H_2/CO = 2:1) at $350\,°C$ for 5 h. After this time, the reactor temperature was lowered until the desired reaction temperature ($300\,°C$) was reached. Subsequently, helium was used to increase the reactor pressure to 2.5 MPa, and the feed gas [H_2 (72 vol%)/CO_2 (24 vol%)/Ar (4 vol% as an internal standard)] was fed into the reactor at a gas hourly space velocity per hour (GHSV) of 2000 mL g^{-1} h^{-1}.

The gaseous products obtained from the CO_2-FTS tests (i.e., CO_2, CO, CH_4, and Ar) were analyzed by online gas chromatography (GC, YL instruments, Korea) with thermal conductivity detection (TCD) and columns packed with Porapak Q and 5 Å molecular sieves. The hydrocarbons C_1 to C_4 were also measured using a flame ionization detector (FID) equipped with a GS-GasPro capillary column.
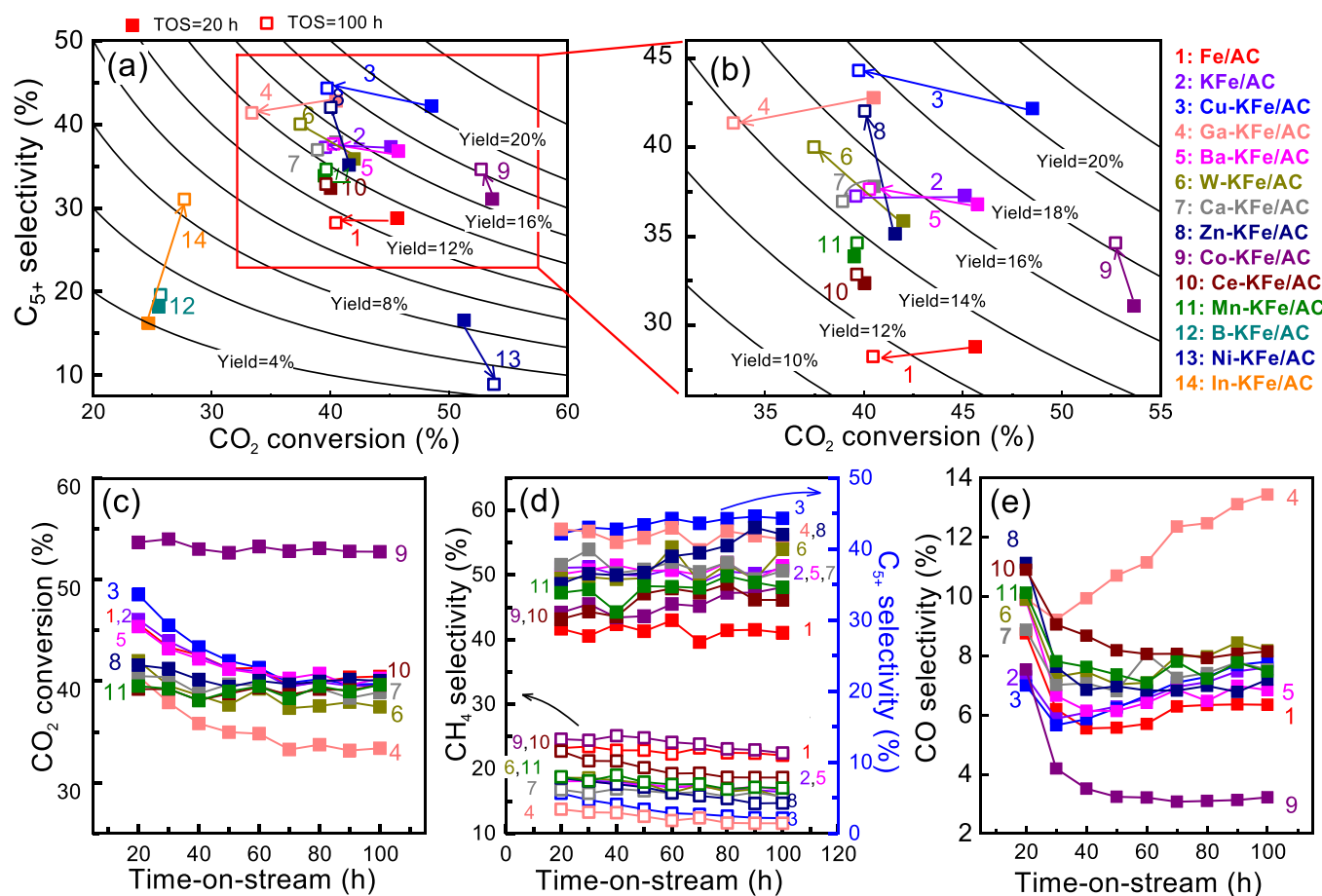
Fig. 1. Performance of Fe/AC catalysts in CO_2 hydrogenation to C_{5+} hydrocarbons. (a) CO_2 conversion and C_{5+} selectivity at the time-on-stream (TOS) of 20 (fill) and 100 h (blank). (b) Enlarged graph for catalysts 1–11. (c) CO_2 conversion, (d) C_{5+} and CH_4 selectivities, and (e) CO selectivity as a function of TOS. Reaction temperature = $300\,°C$, pressure = 2.5 MPa, GHSV = 2000 mL g^{-1} h^{-1}, H_2/CO_2 = 3.

3. Results

3.1. Catalytic activity and product selectivity

Fig. 1(a) and (b) show the C_{5+} yields derived from the CO_2 conversion reaction along with the C_{5+} selectivity at times-on-stream (TOS) of 20 and 100 h for the various catalysts applied in the CO_2-FTS reaction. The reaction results, including further details regarding the product selectivity and the olefin to paraffin ratio (O/P) at a TOS of 60 h, are tabulated in Table S1.

As shown in Fig. 1, the addition of K to the bare Fe/AC was effective in enhancing the C_{5+} selectivity, although a lower CO_2 conversion was obtained (catalysts 1 and 2, Fig. 1). It has been reported that the addition of K to Fe increases the binding strength of C compared to H, thereby accelerating the chain growth reaction [27]. Therefore, K is often expected to act as a selectivity promoter rather than an activity promoter [28]. On the other hand, a large amount of K addition over-dissociates CO_2 or CO, inducing the carbon deposition. In the present study, the addition of K also promotes C_{5+} selectivity to a great extent while CO_2 conversion is slightly lower compared to the bare Fe catalyst, due to the accelerated carbon deposition.

Following the addition of copper as a second metal, the Cu-modified KFe/AC exhibited a significantly higher C_{5+} yield than KFe/AC owing to increases in both the CO_2 conversion and the C_{5+} selectivity at a TOS of 20 h; however, the activity of this catalyst decreased significantly after 100 h on-stream. In contrast, the Ni-modified KFe/AC catalyst exhibited a higher CO_2 conversion than KFe/AC, but it showed a lower C_{5+} selectivity owing to activation of the methanation reaction by Ni. [29, 30]. The decrease in the C_{5+} selectivity for this catalyst became more pronounced as the reaction proceeded. Interestingly, the In- and B-modified catalysts gave lower CO_2 conversions than the bare Fe/AC. Thus, the poor activity of the In-KFe/AC catalyst may originate from its low melting point (157 °C), which induces pore blocking, whereas that of B-KFe/AC may be due to its acidic nature, which inhibits CO_2 adsorption [31].

Furthermore, it was found that the Ca-, Zn-, Co-, Ce-, and Mn-modified catalysts (catalysts 7–11, Fig. 1(b) and (c)) exhibited only slight decreases in their catalytic activities during the reaction, and some of them even showed improved C_{5+} selectivities over time. In contrast, the K-only, Cu, Ga, Ba, and W-modified catalysts (catalysts 2–6, Fig. 1(b) and (c)) exhibited significantly reduced CO_2 conversions during the reaction, although the C_{5+} selectivity was improved compared to the Fe/AC reference catalyst. It is noteworthy that the CO selectivity tended to increase as the reaction proceed, especially for the Ga-added catalyst, suggesting that the active phase changes in a way of decreasing FTS activity consuming CO. (Fig. 1(e)) Since it is well known that the poor stabilities of Fe catalysts impede their practical application, we decided to focus on understanding the factors that lead to catalyst deactivation.

3.2. Physicochemical properties of the catalysts

3.2.1. Catalyst crystal structures

The active phases of the Fe catalyst for the CO_2-FTS can be divided into two phases, namely the Fe_3O_4 and Fe_5C_2 phases, which are responsible for CO_2 activation and growth of the hydrocarbon chains, respectively [8]. It was therefore considered that observing how these phases change during the reaction could help elucidate the cause of catalyst deactivation. Thus, initial powder XRD analyses of the fresh catalysts (Fig. S1(a)) showed characteristic peaks at $2\theta = 30.1$, 35.5, 43.1, and 62.6° (PDF#74–0748), which could be assigned predominantly to Fe_3O_4, while the addition of promoters tended to produce Fe_2O_3 (PDF#88–2359) within the fresh Fe_3O_4. After syngas activation, the Fe oxide phases in the majority of the catalysts were completely reduced and carbonized to iron carbides (Fe_5C_2: 40.8, 42.7, 43.5, 44.2, 45.5, PDF#51–0997; Fe_3C, PDF#03–0989) (Fig. S1(b)). More specifically, the Fe oxides are converted to FeO and then to metallic Fe, prior

to further carbonization to yield Fe carbides [14]. However, in the case of Ga addition, Fe_3O_4 peaks were still detected, indicating that iron oxide was not completely reduced under identical reduction conditions.

The XRD patterns of the used catalysts revealed that the Fe_3O_4 phase was restored, although to different extents depending on the type of promoter (Fig. S1(c)). This can be attributed to the fact that H_2O serves as a mild oxidant during the reaction [15]. More specifically, the Fe_3O_4 peak intensities of the used KFe/AC catalyst and the used W-, Zn-, Ce-, and Mn-modified catalysts were less intense than those of the other used catalysts. As expected, all catalysts exhibited peaks corresponding to iron carbides after the reaction due to the fact that these are widely acknowledged to be the active species, ultimately playing a role in the chain growth reaction during FTS [32–34]. The changes in the active phase content calculated from the XRD peak areas were therefore determined, and are outlined in Fig. 2.

The crystallite size of the catalyst was calculated using the Scherrer equation based on the (311) facet for Fe_3O_4 and the (510) facet for Fe_5C_2. As outlined in Table 1, the crystallite size of the fresh Fe_3O_4 phase was between 30 and 40 nm, while the Mn-modified catalyst exhibited the smallest crystallite size of 25.5 nm. Compared to the reference catalyst Fe/AC, the addition of Mn significantly reduced the particle size, suggesting that the incorporation of Mn could reduce the crystallite size and enhance the dispersion of Fe_3O_4. Additionally, the decreased crystallite sizes observed for the used Fe/AC, KFe/AC, Cu-, and Ga-modified catalysts may be correlated with a phase transformation [13], while the Fe_3O_4 crystallite size increased for the remainder of the catalysts after the reaction due to the likely agglomeration of Fe species [35]. Moreover, the crystallite size of the activated Fe_5C_2 ranged between 15 and 30 nm depending on the promoter, and in all cases, the size increased after the reaction, which may be indicative of sintering.

3.2.2. Textural properties

The degree of exposure of the active phase and the rate of formation of large molecular products can be estimated based on the textural properties of the catalyst. Table 2 outlines the measured N_2 isotherms of the fresh and used catalysts, from which it can be deduced (see Fig. S2) that the N_2 isotherms of the new catalysts exhibit a characteristic irreversible type IV hysteresis loop [36]. This hysteresis loop was classified as Type H3 between relative pressures of 0.5 and 1.0, indicating the presence of mesoporous textural structure. As shown in Table 2, the addition of K significantly reduced the surface area of the catalysts. However, upon the introduction of Ba, Ca, Ce, and Mn promoters into the KFe/AC catalyst, the apparent surface area increased. As indicated by the results presented in Table 1, the addition of these promoters likely increases the dispersion of the catalyst crystallites, and so the large surface area can be attributed to the presence of numerous small crystallites.

Furthermore, the obtained results suggested that the used catalysts exhibited lower surface areas than the fresh catalysts, particularly in the cases of the Fe/AC, KFe/AC, and Zn-modified catalysts. This suggests that the existing products significantly agglomerates after the reaction, and as a result, the pore volumes of the catalysts decreased after the reaction. In this context, Ding et al. [37] postulated two potential explanation for the lower surface area and the larger pore size. More specifically, the formation of magnetite crystallites promotes further agglomeration of the catalyst, thereby reducing the surface area and increasing the pore size. In addition, the carbonaceous species formed on the catalyst can block the pores of the particle network, resulting in a reduction of the BET surface area [37]. These considerations therefore suggest that for the Fe/AC, KFe/AC, and Zn-modified catalysts, the formation of Fe_3O_4 and carbonaceous species may take place to a greater extent on the catalyst surface. These points will be discussed in additional detail later.

3.2.3. Carbonaceous species

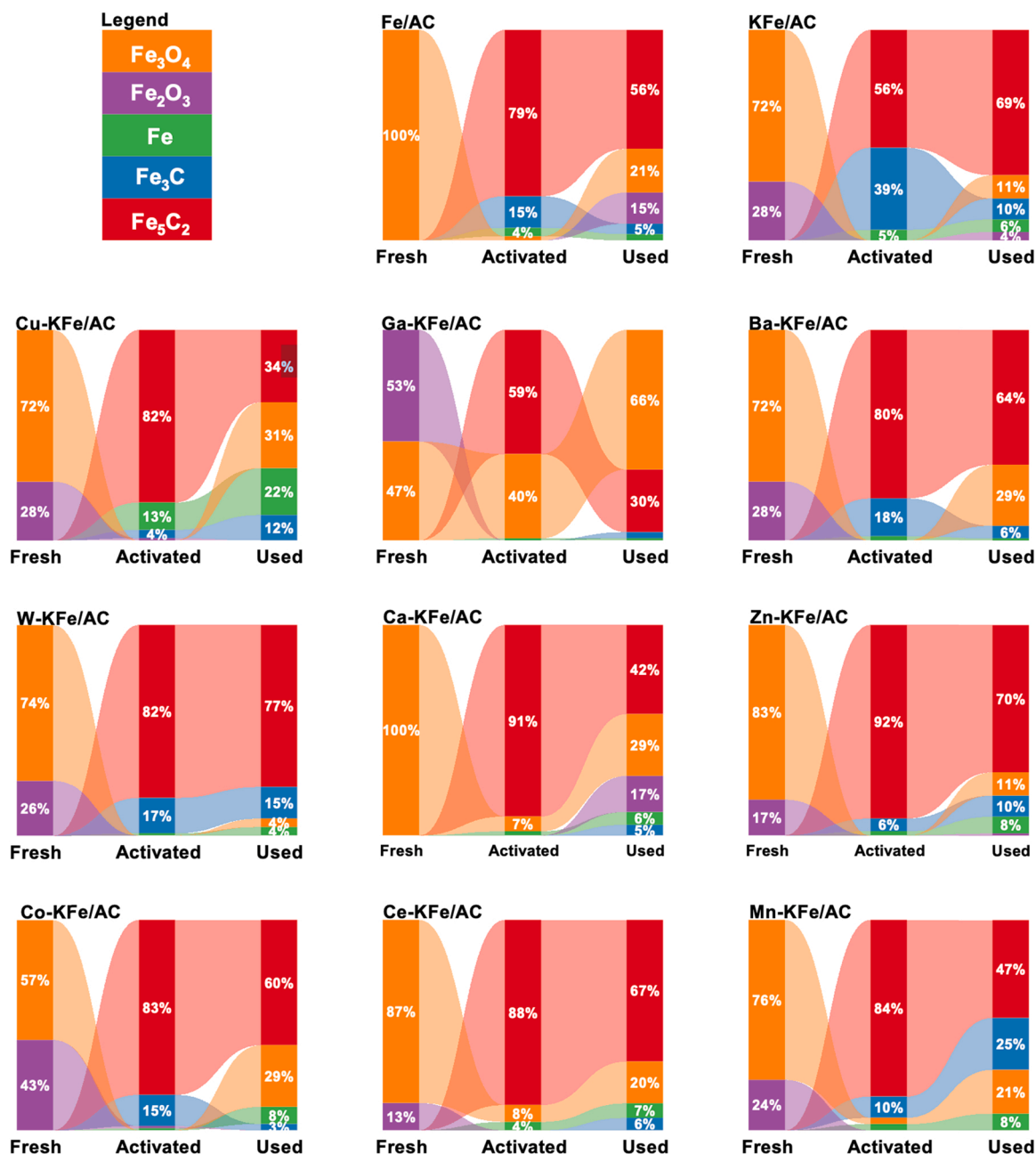Subsequently, Raman spectroscopy (Fig. 3) was used to study the

Fig. 2. Change of Fe phases of fresh (TOS = 0 h), activated (TOS = 20 h), and used (TOS = 100 h) catalysts calculated through the Rietveld refinement.

carbon species present on the surfaces of the various M-KFe/AC catalysts after the reaction, wherein the characteristic peaks at 1350 and 1600 cm^{-1} correspond to the D and G bands of the carbon species in the catalysts, respectively [38,39]. The ratio of the D and G band peak intensities is indicative of the disorder or defect levels of the carbon atoms [14]. As outlined in Table 2, the I_D/I_G ratios for the activated carbon (AC) and fresh Fe/AC catalysts were 1.09 and 1.02, respectively. However, the addition of various promoters decreased the I_D/I_G ratio after the reaction, indicating that all used catalysts, with the exception of the Cu-modified catalyst (I_D/I_G = 1.03), may have formed graphite-like carbon species. More specifically, the Ba-, Co-, Ce-, and Mn-modified catalysts exhibited significantly lower I_D/I_G ratios, suggesting that a greater proportion of graphite carbon was present on these used catalysts. It should be noted here that graphitic carbon is a stable species that is difficult to remove, whereas disordered carbon can be easily hydrogenated in the FTS reaction [40]. This result also indicates that the

Cu-modified catalyst participated in the production of inactive graphitic carbon during the reaction.

The amounts and properties of carbonaceous species grown on the M-KFe/AC catalysts were then further investigated by means of DSC-TG measurements (Fig. 4). The initial mass loss of the AC reference sample below 150 °C was attributed to the evaporation of absorbed water, while the subsequent significant weight loss between 350 and 600 °C originated from the combustion of the AC. For the used Fe/AC catalyst, oxidation of the reduced species led to a small increase in weight between 150 and 250 °C [41]. Notably, decomposition of the carbonaceous compounds that are deposited on the catalyst during the reaction takes place between 250 and 400 °C, as shown in the DSC curve [41]. The degree of carbon deposition listed in Table 2 for each used catalyst (see also Fig. S3). Although these data do not represent the degree of actual carbon deposition because the AC support also burns during the carbon species decomposition process, the obtained values were used to

Table 1

Crystallite sizes of the Fe oxides (fresh and used catalysts) and Fe carbides (activated and used catalysts) calculated from XRD analysis and the Scherrer equation.

Catalyst	Crystallite size (nm)			
	Fe_3O_4		Fe_5C_2	
	Fresh	Used	Activated	Used
Fe/AC	38.5	30.3	18.0	22.4
KFe/AC	33.6	30.6	23.6	30.9
Cu-KFe/AC	43.1	40.9	17.1	17.9
Ga-KFe/AC	35.0	31.2	27.9	28.6
Ba-KFe/AC	33.9	51.0	24.7	29.9
W-KFe/AC	41.6	49.5	16.4	26.7
Ca-KFe/AC	33.6	33.9	19.2	26.1
Zn-KFe/AC	38.1	47.9	16.2	23.9
Co-KFe/AC	37.6	40.6	15.3	25.2
Ce-KFe/AC	37.0	39.0	11.9	22.3
Mn-KFe/AC	25.5	24.2	14.8	30.6

provide a comparison between catalysts. Thus, based on these results, it appeared that a greater degree of carbon deposition took place on the KFe/AC and Zn-modified catalysts, which is consistent with the observed textural properties of the used catalysts described in the preceding section. Ultimately, these results suggest that the formation of carbon species over the KFe/AC and Zn-modified catalysts was accelerated compared to the other catalysts.

In general, the addition of metal promoter alters the basicity of the catalyst surface and hence affect the CO_2 adsorption and dissociation behaviors, which eventually determine a carbon deposition amount [42]. In the present study, CO_2-TPD was performed to measure the surface basicity. As shown in Fig. 5 and Table 2, CO_2 desorption peak was not obvious on bare Fe/AC catalyst, but the addition of K significantly enhanced the surface basicity showing a distinct peak at 705.8 °C, which is associated with the desorption of chemically bound CO_2 [43]. The addition of metal promoters to KFe/AC altered both the temperature and amount of the CO_2 desorption, but interestingly, there was a strong positive correlation between those (Fig. 5(b)). This suggests that the addition of second metal affects the strength and amount of surface basicity in the same direction.

Fig. 5(c) shows the relation between the CO_2 desorption temperature

and the amount of carbon deposited. Although the relation was not such strong, a tendency to deposit a larger amount of carbon at higher desorption temperatures can be confirmed as expected. The influence of basic properties and resulting carbon deposition on deactivation behavior will be discussed in the next section.

4. Discussion

Based on the results obtained following 100 h TOS and subsequent characterization of the used catalyst, the causes of catalyst deactivation were classified into two major factors, namely active site transitions (active phase content and crystallite size) and coke deposition, which manifested differently depending on the promoter employed. However, since these process occur simultaneously during the CO_2-FTS reaction, it remains a challenge to determine which plays the largest role in catalyst deactivation in each system. Thus, in this section, we identify the factors that have the most significant impact on the deactivation behavior and discuss the influence of promoter in terms of overcoming such deactivation.
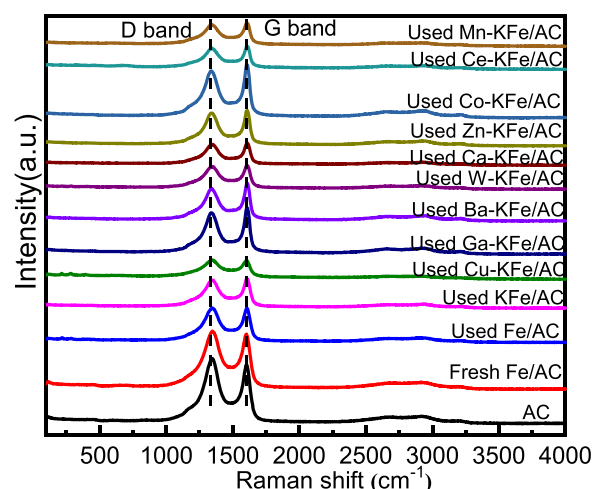

Fig. 3. Raman spectra of the activated carbon, fresh Fe/AC, and used catalysts.

Table 2

Textural properties of the fresh and used catalysts.

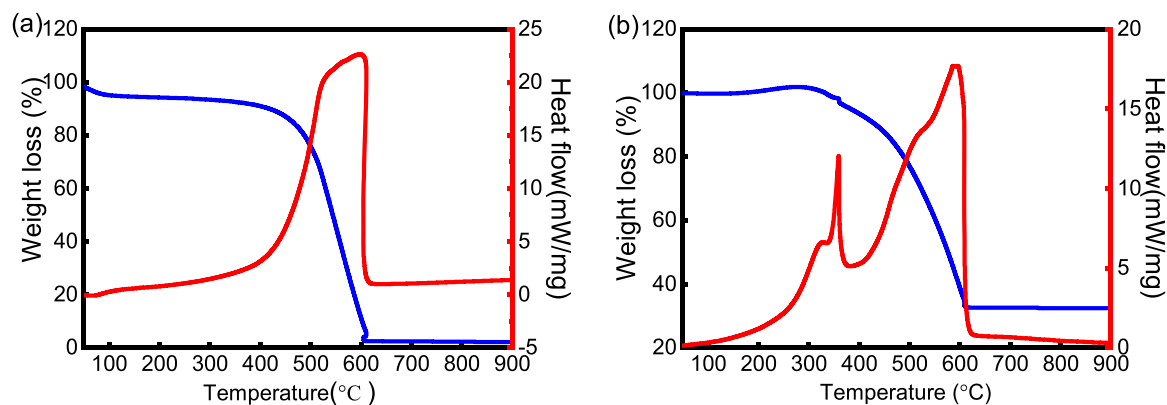| Catalyst	Fresh catalyst			Used catalyst			I_D/I_G	Carbon deposition (wt%)	CO_2 desorption amount (mmol/g)
	Surface area ($m^2 g^{-1}$)	Pore volume ($cm^3 g^{-1}$)	Pore size (nm)	Surface area ($m^2 g^{-1}$)	Pore volume ($cm^3 g^{-1}$)	Pore size (nm)			
AC	920	0.39	3.8	-	-	-	1.09	-	
Fresh Fe/AC	-	-	-	-	-	-	1.02	-	
Fe/AC	681.8	0.33	7.2	56.4	0.10	13.1	0.98	6.60	1.00
KFe/AC	549.7	0.28	6.5	62.6	0.08	8.7	0.92	9.39	6.71
Cu-KFe/AC	522.2	0.26	5.2	133.5	0.13	6.4	1.03	4.87	3.30
Ga-KFe/AC	555.9	0.28	5.2	106.2	0.10	6.3	0.90	6.90	7.86
Ba-KFe/AC	614.5	0.31	5.0	211.9	0.17	5.9	0.84	5.88	7.21
W-KFe/AC	533.7	0.29	5.4	170.7	0.14	5.9	0.91	4.71	7.66
Ca-KFe/AC	627.6	0.31	5.2	208.5	0.16	6.0	0.91	7.07	7.98
Zn-KFe/AC	517.7	0.27	5.1	79.5	0.09	6.1	0.93	9.44	6.96
Co-KFe/AC	500.5	0.26	4.8	133.8	0.13	5.9	0.88	6.07	5.62
Ce-KFe/AC	599.9	0.31	5.1	253.5	0.19	5.6	0.80	7.01	6.89
Mn-KFe/AC	642.5	0.33	5.2	246.8	0.18	5.9	0.86	6.01	7.43

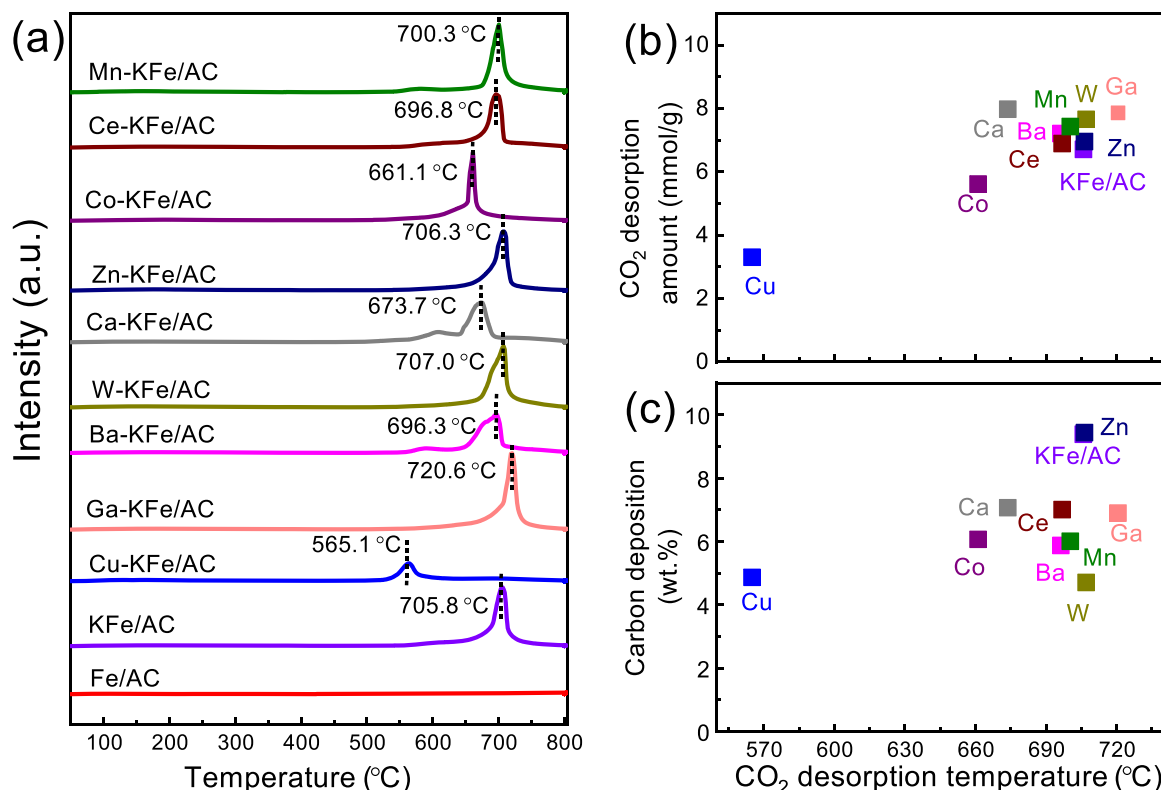**Fig. 4.** DSC and TG curves for (a) the activated carbon, and (b) the used Fe/AC catalyst.

Fig. 5. (a) CO_2-TPD profiles of fresh catalysts, (b) the amount of CO_2 desorption and (c) the carbon deposition as a function of CO_2 desorption temperature.

4.1. Effect of the active site transitions

Since Fe_3O_4 and Fe_5C_2 are known as representative active phases for the initial CO_2 activation (i.e., the RWGS reaction) and chain growth (i. e., Fischer-Tropsch synthesis) processes in this reaction, respectively [32], we attempted to determine the influences of their relative amounts and crystallite sizes on the degree of catalyst deactivation.

Fig. 6(a) shows a heatmap of the Pearson correlation coefficient between variations in the catalyst performance (i.e., ΔCO_2 conversion, ΔC_{5+} yield, and ΔC_{5+} selectivity) and changes in the catalyst properties (i.e., phase content, crystallite size, carbon deposition amount, and textural properties). It should be noted here that the Pearson correlation coefficient indicates the extent of linear correlation between two sets of data and has a value between −1 (strong negative correlation) and 1 (strong positive correlation); the linear regression results for the datasets obtained in our experiments are presented in Fig. 6(b). More specifically, a weak correlation can be seen between the reduction in the CO_2

conversion (ΔCO_2 conversion) and the change in the Fe_5C_2 content (ΔX (Fe_5C_2)) during the reaction (coefficient = −0.09), while a strong correlation was found between the ΔCO_2 conversion and the change in the Fe_5C_2 crystallite size (ΔD(Fe_5C_2), coefficient = 0.84). These results were accounted for by considering that under the thermal and chemical environment of the reaction, the crystallite size of Fe_5C_2 tended to increase (Table 1), thereby inhibiting the CO_2 conversion decreases. This result is in accordance with a previous report that the Fischer-Tropsch activity of Fe carbide is greater when moderately-sized particles rather than small particles are present [44]. Therefore, the Fe_5C_2 crystal growth enhances the Fischer-Tropsch activity, which partially cancels out the negative effect of the oxidation of the active phase.

Fig. 6 also shows the deactivation tendency according to changes in the Fe_3O_4 composition (ΔX(Fe_3O_4)) and the Fe_3O_4 crystallite size (ΔD (Fe_3O_4)). In both cases, no significant correlation was found, thereby suggesting that the chain-growth reaction, in which the intermediate is consumed to produce hydrocarbon species, has a greater influence on
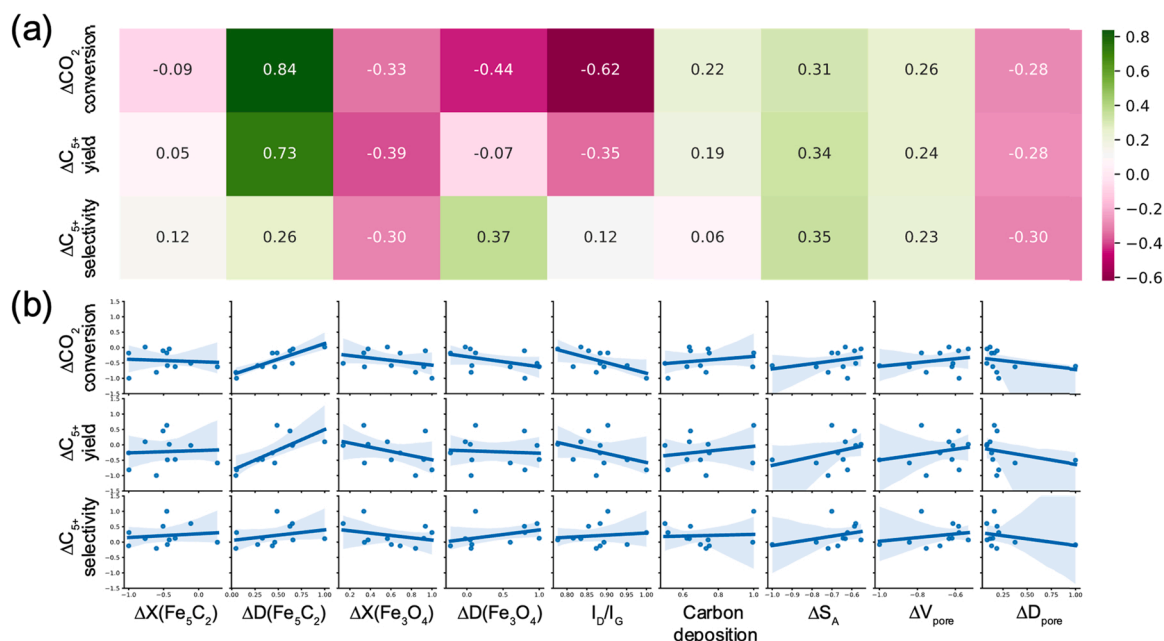
Fig. 6. (a) Pearson correlation coefficients and (b) linear regressions between the changes in the reaction performance and the changes in the catalyst characteristics. ΔCO_2 conversion, ΔC_{5+} yield, and ΔC_{5+} selectivity denote changes in the CO_2 conversion, the C_{5+} yield, and the C_{5+} selectivity, respectively, during TOS from 20 to 100 h. In addition, ΔX, ΔD, I_D/I_G, Carbon deposition, ΔS_A, ΔV_{pore}, and ΔD_{pore} denote the change in the phase content, the change in the crystallite size, the disordered/graphitic carbon ratio obtained from the Raman spectra, the coke amount obtained from DSC-TG measurements, the change in the surface area, the change in the pore volume, and the change in the pore diameter obtained from the N_2 adsorption–desorption isotherms, respectively.

the overall CO_2-FTS activity than on the initial CO_2 activation step [45].

In this context, Wang et al. demonstrated that a higher fraction of the iron carbide phase, particularly χ-Fe_5C_2, promoted the formation of C_2–C_4 olefins and C_{5+} hydrocarbons [46]. In the present study, it was found that the addition of Cu, Ga, and Ba promoters resulted in a significant decrease in the CO_2 conversion with a large reduction in the Fe_5C_2 phase content (Fig. 2). However, although the Ca- and Zn-modified catalysts exhibited similar decreases in activity (ΔCO_2 conversions of −1.59 and −1.54%, respectively), their Fe_5C_2 content changes were quite different (i.e., $\Delta X(Fe_5C_2)$ of − 48 and − 22%, respectively). We therefore considered that this discrepancy is due to the increased Fe_5C_2 crystallite size, as described above. Although the oxidation of Fe carbide is a sign of deactivation, the large increase in crystallite size may have compensated for the deactivation process, ultimately slowing the deactivation process.

Since the XRD results represent only the bulk phase information, XPS of Fe2p was additionally performed to characterize the surface chemical composition and electronic properties. As shown in Fig. 7, four typical

catalysts (Fe/AC, KFe/AC, Cu-KFe/AC, and Zn-KFe/AC) with high CO_2 conversion and different deactivation rates were selected. Peaks appeared at 711 eV (satellited at 715 eV) and 724 eV (satellited at 728 eV) correspond to $Fe2P_{3/2}$ and $Fe2p_{1/2}$ of Fe^{3+}, respectively, indicating iron oxides (FeOx) on the surface [47]. Peaks appeared at ~707 eV and ~720 eV was assigned to iron carbide (FeCx) species [48, 49].

To quantify the change in surface oxidation state during the reaction, the peak area ratio of FeC_x/FeO_x was calculated for catalysts collected at the activated and used stage (Fig. 7(c)). The ratio of all catalysts decreased during the reaction except the Zn-modified catalyst, which showed almost constant FeC_x/FeO_x ratio. Apparently, the Cu-modified catalyst showed the highest FeC_x/FeO_x ratio at the activated stage, but it significantly decreased after the reaction. In accordance with bulk structure analysis, it is confirmed again that the catalyst surface undergoes the oxidation process during the CO_2 hydrogenation reaction and the phase transition of the Cu-modified catalyst is more distinctive compared to others.
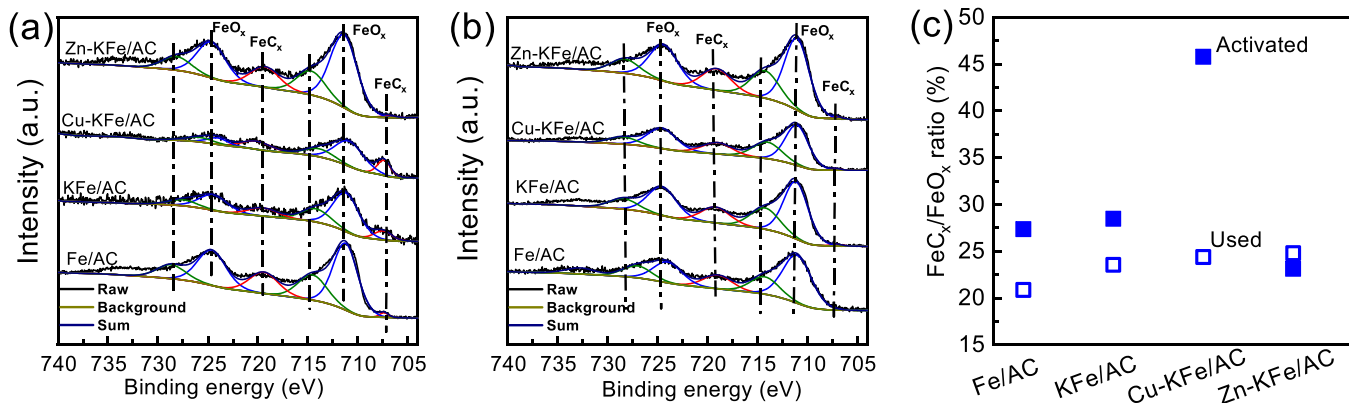
Fig. 7. XPS spectra of Fe 2p in (a) activated and (b) used catalysts. Zn-KFe/AC, Cu-KFe/AC, KFe/AC and Fe/AC were surveyed. (c) FeCx/FeOx peak area ratios are present.

The increase in CO selectivity as the reaction proceeds is further evidence that high FeO_X content is a sign of deactivation feature (Fig. 1 (e)), according to the two-step mechanism, RWGS followed by FTS [14]. Since FeOx and FeCx phases are responsible for RWGS and FTS [32], respectively, the phase transition from FeCx to FeOx promotes CO production while suppressing its subsequent consumption, resulting in higher net CO production.

4.2. Effect of carbon deposition on the catalytic performance

The deposition of carbonaceous species also plays a significant role in determining the catalytic activity, as inactive carbonaceous compounds can limit the contact between the reactants and the active sites [19,20,50]. Thus, Fig. 6 depicts how the crystallinity of the carbon species (i.e., I_D/I_G) and the amount of carbonaceous compounds (i.e., carbon deposition) are related to the deactivation behavior of the CO_2-FTS reaction. More specifically, it can be seen that the I_D/I_G ratio appears to have a stronger relationship with the ΔCO_2 conversion value than the amount of deposited carbonaceous species. In addition, catalysts showing a rapid deactivation rate tend to possess large I_D/I_G ratios, suggesting that the deposition of disordered carbon species on the active sites has a large impact on deactivation.

However, the amount of deposited coke did not show a clear relationship with the degree of deactivation, which implies that even if carbonaceous species are deposited to some extent, they do not necessarily impair the mass transfer property of the catalyst if a sufficient amount of disorder is present in the carbon structure. In fact, this result contradicts that of a previous study, in which the disordered carbon did not affect the FT reaction due to its ability to undergo hydrogenation [40]. In the same context, the I_D/I_G ratio has limitations in accurately explaining the relationship between carbon deposition and deactivation. For instance, the KFe/AC and Zn-KFe/AC catalysts exhibit the most severe carbon deposition of the various catalysts examined (i.e., 9.39 and 9.44 wt%, respectively), and both catalysts possess similar I_D/I_G ratios (0.92). However, the former undergoes rapid deactivation, while the latter maintains a stable catalytic activity and its C_{5+} yield increases over time. These observations suggest that carbon deposition and the consequent decrease in surface area have less of an effect on deactivation than the intrinsic decrease in activity due to changes in the active site transitions. The relatively weak correlation between the disordered carbon and deactivation rate is presumably due to its indirect influence on the catalysis, that is, the disordered carbons can serve as a hydrogen reservoir [51] and create a hydrogen-deficient environment in adjacent

active sites to further accelerate the phase transition.

4.3. Identification of the promoter effect on the catalyst stability

The activities, stabilities, and product selectivities of the 10 different elements used as promoters and those of the modified Fe/AC catalysts were found to differ significantly. Thus, in combination with the obtained characterization results, we depicted the overall trend for each catalyst in terms of the factors responsible for catalyst deactivation (i.e., active site transitions, including active phase and active crystallite size changes, and carbon deposition). Typically, as the reaction time increases, the catalyst undergoes changes in its active phase, and carbon deposition occurs with relative ease. When these changes occur during the reaction, one or more could lead to catalyst deactivation. Thus, the deactivation behavior of each catalyst is discussed in greater detail in the following paragraphs. Fig. 8 shows a schematic representation of the potential deactivation routes (i.e., active phase changes, active crystallite size changes, and carbon deposition) considered in this study.

Prior to discussing the deactivation behaviors of the various catalysts, it should be noted that the Zn-, Co-, Mn-, Ce-, and Ca-modified catalysts demonstrated excellent activities, stabilities, and C_{5+} selectivities. However, after the reaction, the Mn-modified catalyst exhibited a significant decrease in the Fe_5C_2 phase content, and Fig. 2 reveals that the majority of this component was converted to Fe_3C. To the best of our knowledge, both Fe_5C_2 and Fe_3C are the most prevalent iron carbides during the FTS; however, the role of Fe_3C remains unclear. In this context, Herranz et al. proposed that θ-Fe_3C species are less active in the FTS than χ-Fe_5C_2 species [52]. However, Ma et al. reported that θ-Fe_3C was active in the FTS, and that it exhibited a superior C–C chain growth ability to yield a higher C_{5+} selectivity [53]. Accordingly, for the Mn-modified catalyst, we found a decrease in the Fe_5C_2 phase content and a slight increase in the Fe_3O_4 content, whereas the actual phase transformation from Fe_5C_2 to Fe_3C appeared to have a negligible effect on CO_2 conversion and the C_{5+} yield. We hypothesized that the increased crystallite size of Fe_5C_2 exposed a greater number of active sites, which remained stable to prevent catalyst deactivation. Therefore, although the amount of active phase Fe_5C_2 decreased during the reaction, the phase transformation from Fe_5C_2 to Fe_3C did not result in deactivation of the catalyst, and the increased crystallite size of the active species may even enhance the catalyst stability.

Typically, the addition of Co is known to boost the catalytic activity and C_{2+} yield by modulating the H* /CO* species ratio or the hydrogenation ability [29]. If the reaction pathway involves a CO-mediated
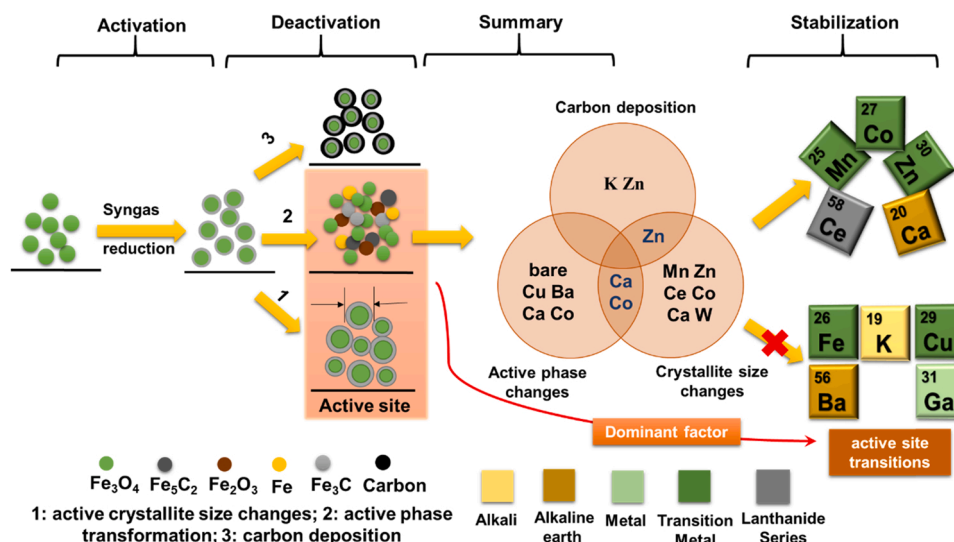

Fig. 8. Schematic representation of the deactivation behavior over different promoters.

route for CO_2 hydrogenation, abundant CO^* chemisorption would be expected to play a crucial role, and so a Co-based catalyst would be an ideal candidate [54]. In addition to a decreasing content of the active iron phase, the Co-modified catalyst also exhibited a decreasing trend in Fe_5C_2 phase content; however, the catalyst activity remained relatively stable (ΔCO_2 conversion = 0.93%) up to a TOS of 100 h. This stability was partly attributed to the fact that although the active Fe_5C_2 phase content decreased, the size of the active crystallites increased significantly, which enhanced the stability of the catalyst. In addition, Co could act as an active site for CO (an intermediate in the reaction), ultimately leading to a superior CO_2 conversion. However, because of the higher H/C ratio and the lower CO partial pressure, methane formation and the secondary reactions of light olefins are favored [54], resulting in a higher CH_4 selectivity and the production of saturated hydrocarbons (see Table S1). It was also evident that the C_{5+} yield increased following the reaction over this catalyst. As previously reported, a closer intimate distance between the Fe and Co sites, especially during formation of the FeCo alloy, results in a greater the C_{5+} selectivity [55]. In the present study, the formation of FeCo alloy was observed as well. The HR-TEM image of the used Co-FeK/AC (Fig. S4(a)) shows that the lattice fringe of 0.205 nm, which is assigned to the (110) plane of the FeCo alloy. The HAADF-STEM and EDS element mapping (Fig. S4(b)) show that Fe and Co elements were in close contact with an even distribution. These observations indicate the formation of FeCo alloy, which alter the adsorption capability and improve catalyst stability and long-chain hydrocarbons selectivity [56].

Ce is known to enhance the WGS and RWGS reactions, which is advantageous for the CO_2-FTS reaction owing to its ability to activate the CO_2 to CO transformation [57,58]. Based on the results of the CO_2-FTS reaction, it appeared that the Ce-modified catalyst exhibited minimal changes in the CO_2 conversion and C_{5+} selectivity over time. Previously, it was suggested that Ce may prefer to deposit on the support instead of on the active iron particles, thereby increasing the number of active sites [59]. In addition, Nie et al. [60] discovered that the addition of Ce increased the BET surface area and inhibited H_2 adsorption. Owing to its ability to donate electrons, the introduction of a suitable quantity of Ce promotes the carbonization process. Indeed, based on the above results, it was found that the Ce-modified catalyst exhibited the lowest I_D/I_G ratio and a moderate degree of carbon deposition, but continued to maintain a higher iron carbide phase content and a larger increasing trend of Fe_5C_2 crystallite size, ultimately resulting in a stable activity and a good C_{5+} yield. This indicates that carbon deposition on the catalyst had a negligible effect on its activity. However, the minimal change in the active phase and the growth of the active crystallite size stabilized the CO_2 conversion and the C_{5+} yield.

Introduction of Zn not only promotes CO_2 adsorption and the formation of a greater proportion of basic iron carbides [29], but also can inhibit the oxidation of Fe_xC_y and stabilize Fe-based catalysts [14,61]. Based on our findings, it was clear that the Zn-modified catalyst demonstrated a slight decrease in CO_2 conversion and an upward trend in the C_{5+} yield (see Fig. 1). Moreover, compared to the other stabilized catalysts (i.e., those containing Co, Ce, Ca, and Mn), the Zn-modified catalyst exhibited a lower CO selectivity and a significantly higher O/P ratio (2.41). These results suggest that the formation of C_2–C_4 olefins and C_{5+} hydrocarbons was enhanced by the presence of a higher proportion of the iron carbide phase, particularly χ-Fe_5C_2 [46].

Despite the lower surface area and severe degree of carbon deposition, this catalyst exhibited a higher Fe_5C_2 phase content and an increasing active crystallite size in its activated and used forms. It was therefore hypothesized that Zn-modified catalysts can produce greater amounts of iron carbide species when treated with syngas, and that they also inhibit oxidation during the reaction, ultimately improving the catalyst stability and enhancing the chain growth capability. Notably, it was also confirmed that maintaining a higher active site content (i.e., a high active phase content and an increasing active crystallite size) can stabilize the catalyst activity, and in this case, carbon deposition has

only a minor effect on the deactivation behavior. Previous study [14] suggested how Zn stabilizes FeC_x phase during the CO_2 hydrogenation reaction. They observed that Zn easily migrates to the Fe surface and it serves as a sacrificial oxidation agent forming ZnO, which prevents the oxidation of FeC_x by CO_2 and H_2O in the stream. We also identified the ZnO located at the Fe surface as shown in Fig. S5 in the Supporting Information. Unlike the used Co-FeK/AC (Fig. S4), the used Zn-FeK/AC showed that the positions of Fe and Zn were not perfectly matched, and Zn and O were distributed over a wider area than Fe. The outer region continued to detect ZnO (101) formation with lattice fringes of 0.241 nm, as shown by the HR-TEM image. Therefore, in the present study as well, both the migration of Zn to the Fe surface and the formation of ZnO effectively inhibited the oxidation of FeC_x of Zn-KFe/AC.

Finally, the influence of W modification was evaluated. It was found that this catalyst maintained a stable C_{5+} yield (i.e., 15.1–15.0% upon increasing the TOS from 20 to 100 h), in addition to exhibiting higher O/P values with minimal changes in the active phase content and the Fe_5C_2 concentration. As a result, the resulting product distribution matches the Fe_5C_2 phase content. However, it was found that the catalyst activity decreased over the course of 100 h, and the CH_4 yield exhibited a decreasing trend. This reduced conversion of CO_2 was therefore attributed to the fact that although that the active phase content was maintained at a higher level, the crystallite size deviated (Fig. 6(b)); however, the stable C_{5+} yield remains a mystery. Accordingly, studies are ongoing in our group regarding the deactivation behavior of the W-modified catalyst, and the results will be presented in due course.

In summary, the deactivation of Fe catalyst was delayed through the addition of metal promoters. Bare Fe/AC catalyst, showed a rapid decrease in CO_2 conversion and a large loss of Fe carbide content but little increase in crystallite size. When metal promoters were added, some of them showed positive behavior in terms of catalyst stability. What they showed in common was a high content of active Fe carbide and its large size. Other metal-modified catalysts with severe oxidation of Fe carbide showed significant decreases in CO_2 conversions during the reaction.

5. Conclusion

The deactivation behaviors of Fe-based catalysts supported on active carbon were investigated using a range of metal promoters, and the resulting catalytic activities and selectivities over the course of a 100 h reaction were evaluated. Based on plots of the key factors affecting the catalytic performance, it was found that 11 catalysts were partially inactive following the reaction owing to changes in their active sites. Although the oxidation of Fe carbides plays a dominant role in the deactivation process, an increase in the crystallite size of the active Fe_5C_2 species readily exposes a greater number of active sites to compensate for the deactivation by the oxidation. In addition, it was found that carbon deposition on the catalyst had only a minor effect on the deactivation behavior, but we cannot be fully ruled out that will be a vital role for the extension of the catalyst lifetime. In terms of the Cu-promoted catalyst, a higher CO_2 conversion (41.3%) and C_{5+} selectivity (44.3%) were obtained compared to the un-modified Fe/AC catalyst; however, the catalytic activity was less stable owing to changes in the active sites (i.e., active phase and active crystallite size changes) during the reaction. Additionally, deactivation of the Fe/AC and KFe/AC catalysts and of the Ga- and Ba-promoted catalysts appeared to occur for the same reason. However, in contrast, the Mn-, Ce-, and Zn-promoted catalysts maintained higher iron carbide phase contents and readily exposed active sites owing to the increasing trend in crystallite size, thereby resulting in a stable CO_2 conversion. Although the Ca, and Co-promoted catalyst existed oxidation of Fe carbide, the large increment of crystallite size alleviated the deactivation process. Moreover, among the 10 different promoters evaluated herein, the Zn-modified catalyst was the most effective at protecting the active sites, and it demonstrated stable activation along with an excellent performance for the production

of light olefins and C_{5+} hydrocarbons.

CRediT authorship contribution statement

Jingyu Chen: Writing – original draft, Investigation, Data curation. **Seung Ju Han**: Formal analysis. **Hae-Gu Park:** Investigation. **Khasan Nasriddinov:** Data curation. **Chundong Zhang:** Formal analysis. **Ki-Won Jun:** Project administration, Funding acquisition, Supervision. **Seok Ki Kim:** Project administration, Supervision, Writing – review & editing.

Declaration of Competing Interest

The authors declare the following financial interests/personal relationships which may be considered as potential competing interests: Ki-Won Jun reports financial support was provided by National Research Foundation of Korea.

Data availability

Data will be made available on request.

Acknowledgments

Appendix A. Supporting information

Supplementary data associated with this article can be found in the online version at doi:10.1016/j.apcatb.2023.122370.

References

[1] R. Gao, C. Zhang, K.-W. Jun, S.K. Kim, H.-G. Park, T. Zhao, L. Wang, H. Wan, G. Guan, Green liquid fuel and synthetic natural gas production via CO_2 hydrogenation combined with reverse water-gas-shift and co-based Fischer-Tropsch synthesis, J. CO_2 Util. 51 (2021), 101619, https://doi.org/10.1016/j.jcou.2021.101619.

[2] Y.H. Choi, Y.J. Jang, H. Park, W.Y. Kim, Y.H. Lee, S.H. Choi, J.S. Lee, Carbon dioxide Fischer-Tropsch synthesis: a new path to carbon-neutral fuels, Appl. Catal. B 202 (2017) 605–610, https://doi.org/10.1016/j.apcatb.2016.09.072.

[3] T. Witoon, V. Lapkeaseree, T. Numpilai, C.K. Cheng, J. Limtrakul, CO_2 hydrogenation to light olefins over mixed Fe-Co-K-Al oxides catalysts prepared via precipitation and reduction methods, Chem. Eng. J. 428 (2022), 131389, https://doi.org/10.1016/j.cej.2021.131389.

[4] Z. Liu, X. Gao, B. Liu, W. Song, Q. Ma, T. sheng Zhao, X. Wang, J.W. Bae, X. Zhang, J. Zhang, Highly stable and selective layered Co-Al-O catalysts for low-temperature CO_2 methanation, Appl. Catal. B 310 (2022), 121303, https://doi.org/10.1016/j.apcatb.2022.121303.

[5] S. Kar, R. Sen, A. Goeppert, G.K.S. Prakash, Integrative CO_2 capture and hydrogenation to methanol with reusable catalyst and amine: toward a carbon neutral methanol economy, J. Am. Chem. Soc. 140 (2018) 1580–1583, https://doi.org/10.1021/jacs.7b12183.

[6] R. Gao, C. Zhang, K.-W. Jun, S.K. Kim, H.-G. Park, T. Zhao, L. Wang, H. Wan, G. Guan, Transformation of CO_2 into liquid fuels and synthetic natural gas using green hydrogen: a comparative analysis, Fuel 291 (2021) 120111, https://doi.org/10.1016/j.fuel.2020.120111.

[7] P. Schmidt, V. Batteiger, A. Roth, W. Weindorf, T. Raksha, Power-to-liquids as renewable fuel option for aviation: a review, Chem. Ing. Tech. 90 (2018) 127–140, https://doi.org/-10.1002/cite.201700129.

[8] C. Panzone, R. Philippe, A. Chappaz, P. Fongarland, A. Bengaouer, Power-to-liquid catalytic CO_2 valorization into fuels and chemicals: focus on the Fischer-Tropsch route, J. CO_2 Util. 38 (2020) 314–347, https://doi.org/10.1016/j.jcou.2020.02.009.

[9] J. Wei, R. Yao, Y. Han, Q. Ge, J. Sun, Towards the development of the emerging process of CO_2 heterogenous hydrogenation into high-value unsaturated heavy hydrocarbons, Chem. Soc. Rev. 50 (2021) 10764–10805, https://doi.org/10.1039/D1CS00260K.

[10] J. Liu, A. Zhang, X. Jiang, M. Liu, Y. Sun, C. Song, X. Guo, Selective CO_2 hydrogenation to hydrocarbons on Cu-promoted Fe-based catalysts: dependence on Cu–Fe interaction, ACS Sustain. Chem. Eng. 6 (2018) 10182–10190, https://doi.org/10.1021/acssuschemeng.-8b01491.

[11] J. Li, Y. He, L. Tan, P. Zhang, X. Peng, A. Oruganti, G. Yang, H. Abe, Y. Wang, N. Tsubaki, Integrated tuneable synthesis of liquid fuels via Fischer–Tropsch technology, Nat. Chem. 1 (2018) 787–793, https://doi.org/10.1038/s41929-018-0144-z.

[12] J. Zhang, S. Lu, X. Su, S. Fan, Q. Ma, T. Zhao, Selective formation of light olefins from CO_2 hydrogenation over Fe–Zn–K catalysts, J. CO_2 Util. 12 (2015) 95–100, https://doi.org/-10.1016/j.jcou.2015.05.004.

[13] S.-M. Hwang, C. Zhang, S.J. Han, H.-G. Park, Y.T. Kim, S. Yang, K.-W. Jun, S. K. Kim, Mesoporous carbon as an effective support for Fe catalyst for CO_2 hydrogenation to liquid hydrocarbons, J. CO_2 Util. 37 (2020) 65–73, https://doi.org/10.1021/acscentsci.0c00976.

[14] C. Zhang, C. Cao, Y. Zhang, X. Liu, J. Xu, M. Zhu, W. Tu, Y.-F. Han, Unraveling the role of zinc on bimetallic Fe_5C_2–ZnO catalysts for highly selective carbon dioxide hydrogenation to high carbon α-olefins, ACS Catal. 11 (2021) 2121–2133, https://doi.org/10.1021/acscatal.0c04627.

[15] Y. Zhang, C. Cao, C. Zhang, Z. Zhang, X. Liu, Z. Yang, M. Zhu, B. Meng, J. Xu, Y.-F. Han, The study of structure-performance relationship of iron catalyst during a full life cycle for CO_2 hydrogenation, J. Catal. 378 (2019) 51–62, https://doi.org/10.1016/j.jcat.2019.08.001.

[16] J.-S. Hong, J.S. Hwang, K.-W. Jun, J.C. Sur, K.-W. Lee, Deactivation study on a coprecipitated Fe-Cu-K-Al catalyst in CO_2 hydrogenation, Appl. Catal. A Gen. 218 (2001) 53–59, https://doi.org/10.1016/S0926860X(01)00617-2.

[17] P.S. Sai Prasad, J.W. Bae, K.-W. Jun, K.-W. Lee, Fischer–Tropsch synthesis by carbon dioxide hydrogenation on Fe-based catalysts, Catal. Surv. Asia 12 (2008) 170–183, https://doi.org/10.1007/s10563-008-9049-1.

[18] V.R.R. Pendyala, U.M. Graham, G. Jacobs, H.H. Hamdeh, B.H. Davis, Fischer–Tropsch synthesis: morphology, phase transformation, and carbon-layer growth of iron-based catalysts, ChemCatChem 6 (2014) 1952–1960, https://doi.org/10.1002/cctc.201402073.

[19] E. de Smit, B.M. Weckhuysen, The renaissance of iron-based Fischer–Tropsch synthesis: on the multifaceted catalyst deactivation behaviour, Chem. Soc. Rev. 37 (2008) 2758–2781, https://doi.org/10.1039/B805427D.

[20] A. Ochoa, J. Bilbao, A.G. Gayubo, P. Castaño, Coke formation and deactivation during catalytic reforming of biomass and waste pyrolysis products: a review, Renew. Sustain. Energy Rev. 119 (2020), 109600, https://doi.org/10.1016/j.rser.2019.109600.

[21] J. Artz, T.E. Müller, K. Thenert, J. Kleinekorte, R. Meys, A. Sternberg, A. Bardow, W. Leitner, Sustainable conversion of carbon dioxide: an integrated review of catalysis and life cycle assessment, Chem. Rev. 118 (2018) 434–504, https://doi.org/10.1021/acs.chemrev.7b00435.

[22] S. Abelló, D. Montané, Exploring iron-based multifunctional catalysts for Fischer–Tropsch synthesis: a review, ChemSusChem 4 (2011) 1538–1556, https://doi.org/10.1002/cssc.-201100189.

[23] J.S. Hwang, K.-W. Jun, K.-W. Lee, Deactivation and regeneration of Fe-K/alumina catalyst in CO_2 hydrogenation, Appl. Catal. A Gen. 208 (2001) 217–222, https://doi.org/10.1016/S0926-860X(00)00701-8.

[24] T. Wang, Y. Xu, Y. Li, L. Xin, B. Liu, F. Jiang, X. Liu, Sodium-mediated bimetallic Fe–Ni catalyst boosts stable and selective production of light aromatics over HZSM-5 zeolite, ACS Catal. 11 (2021) 3553–3574, https://doi.org/10.1021/acscatal.1c00169.

[25] N. Bashiri, M.R. Omidkhah, H.R. Godini, Direct conversion of CO_2 to light olefins over FeCo/XK-YAL$_2$O$_3$ (X= La, Mn, Zn) catalyst via hydrogenation reaction, Res. Chem. Intermed. 47 (2021) 5267–5289, https://doi.org/10.1007/s11164-021-04562-z.

[26] W. Ma, E.L. Kugler, J. Wright, D.B. Dadyburjor, Mo− Fe catalysts supported on activated carbon for synthesis of liquid fuels by the Fischer− Tropsch process: effect of Mo addition on reducibility, activity, and hydrocarbon selectivity, Energy Fuels 20 (2006) 2299–2307, https://doi.org/10.1021/ef0602372.

[27] S.-M. Hwang, S.J. Han, J.E. Min, H.-G. Park, K.-W. Jun, S.K. Kim, Mechanistic insights into Cu and K promoted Fe-catalyzed production of liquid hydrocarbons via CO_2 hydrogenation, J. CO_2 Util. 34 (2019) 522–532, https://doi.org/10.1016/j.jcou.2019.08.004.

[28] S.R. Yan, K.W. Jun, J.S. Hong, M.J. Choi, K.W. Lee, Promotion effect of Fe-Cu catalyst for the hydrogenation of CO_2 and application to slurry reactor, Appl. Catal. A Gen. 194 (2000) 63–70, https://doi.org/10.1016/S0926-860X(99)00354-3.

[29] L. Guo, J. Li, Y. Zeng, R. Kosol, Y. Cui, N. Kodama, X. Guo, R. Prasert, V. Tharapong, G. Liu, Heteroatom doped iron-based catalysts prepared by urea self-combustion method for efficient CO_2 hydrogenation, Fuel 276 (2020), 118102, https://doi.org/10.1016/j.fuel.2020.118102.

[30] K. Zhao, W. Wang, Z. Li, Highly efficient Ni/ZrO$_2$ catalysts prepared via combustion method for CO_2 methanation, J. CO_2 Util. 16 (2016) 236–244, https://doi.org/10.1016/j.jcou.2016.07.-010.

[31] Y.O.U. Zhenya, D. Weiping, Q. ZHANG, W. Ye, Hydrogenation of carbon dioxide to light olefins over non-supported iron catalyst, Chin. J. Catal. 34 (2013) 956–963, https://doi.org/-10.1016/S1872-2067(12)60559-2.

[32] B. Yao, T. Xiao, O.A. Makgae, X. Jie, S. Gonzalez-Cortes, S. Guan, A.I. Kirkland, J. R. Dilworth, H.A. Al-Megren, S.M. Alshihri, Transforming carbon dioxide into jet fuel using an organic combustion-synthesized Fe-Mn-K catalyst, Nat. Chem. 11 (2020) 1–12, https://doi.org/-10.1038/s41467-020-20214-z.

[33] C. Yang, H. Zhao, Y. Hou, D. Ma, Fe_5C_2 nanoparticles: a facile bromide-induced synthesis and as an active phase for Fischer–Tropsch synthesis, J. Am. Chem. Soc. 134 (2012) 15814–15821, https://doi.org/10.1021/ja305048p.

[34] J. Liu, A. Zhang, X. Jiang, M. Liu, J. Zhu, C. Song, X. Guo, Direct transformation of carbon dioxide to value-added hydrocarbons by physical mixtures of Fe_5C_2 and K-modified Al$_2$O$_3$, Ind. Eng. Chem. Res. 57 (2018) 9120–9126, https://doi.org/10.1021/acs.iecr.8b02017.

[35] Y. Zhang, M. Qing, H. Wang, X.-W. Liu, S. Liu, H. Wan, L. Li, X. Gao, Y. Yang, X.-D. Wen, Comprehensive understanding of SiO$_2$-promoted Fe Fischer-Tropsch synthesis catalysts: Fe-SiO$_2$ interaction and beyond, Catal. Today 368 (2021) 96–105, https://doi.org/10.1016/-j.cattod.2020.02.026.

[36] Z. Di, X. Feng, Z. Yang, M. Luo, Effect of iron precursor on catalytic performance of precipitated iron catalyst for Fischer–Tropsch synthesis reaction, Catal. Lett. 150 (2020) 2640–2647, https://doi.org/10.1007/s10562-020-03158-3.

[37] M. Ding, Y. Yang, J. Xu, Z. Tao, H. Wang, H. Wang, H. Xiang, Y. Li, Effect of reduction pressure on precipitated potassium promoted iron–manganese catalyst for Fischer–Tropsch synthesis, Appl. Catal. A Gen. 345 (2008) 176–184, https://doi.org/10.1016/j.apcata.2008.04.036.

[38] L. Niu, X. Liu, X. Wen, Y. Yang, J. Xu, Y. Li, Effect of potassium promoter on phase transformation during H$_2$ pretreatment of a Fe$_2$O$_3$ Fischer Tropsch synthesis catalyst precursor, Catal. Today 343 (2020) 101–111, https://doi.org/10.1016/j.cattod.2019.01.054.

[39] A.C. Ferrari, J. Robertson, Interpretation of Raman spectra of disordered and amorphous carbon, Phys. Rev. B 61 (2000) 14095, https://doi.org/10.1103/PhysRevB.61.14095.

[40] W. Chen, T.F. Kimpel, Y. Song, F.-K. Chiang, B. Zijlstra, R. Pestman, P. Wang, E.J. M. Hensen, Influence of carbon deposits on the cobalt-catalyzed Fischer–Tropsch reaction: evidence of a two-site reaction model, ACS Catal. 8 (2018) 1580–1590, https://doi.org/10.1021/acscatal.-7b03639.

[41] M. Russo, V. La Parola, M.L. Testa, G. Pantaleo, A.M. Venezia, R.K. Gupta, A. Bordoloi, R. Bal, Structural insight in TiO$_2$ supported CoFe catalysts for Fischer–Tropsch synthesis at ambient pressure, Appl. Catal. A Gen. 600 (2020), 117621, https://doi.org/10.1016/j.apcata.2020.117621.

[42] O.O. James, B. Chowdhury, S. Maity, Comparative TPR and TPD studies of Cu and Ca promotion on Fe-Zn- and Fe-Zn-Zr-based Fischer-Tropsch catalysts, Oil Gas Sci. Technol. Rev. IFP Energ. Nouv. 70 (2015) 511–519, https://doi.org/10.2516/-ogst/2013114.

[43] Z. Han, W. Qian, H. Zhang, H. Ma, Q. Sun, W. Ying, Effect of rare-earth promoters on precipitated iron-based catalysts for Fischer-Tropsch synthesis, Ind. Eng. Chem. Res. 59 (2020) 14598–14605, https://doi.org/10.1021/acs.iecr.9b06760.

[44] H.M. Torres Galvis, J.H. Bitter, T. Davidian, M. Ruitenbeek, A.I. Dugulan, K.P. de Jong, Iron particle size effects for direct production of lower olefins from synthesis gas, J. Am. Chem. Soc. 134 (2012) 16207–16215, https://doi.org/10.1021/ja304958u.

[45] T. Riedel, H. Schulz, G. Schaub, K.-W. Jun, J.-S. Hwang, K.-W. Lee, Fischer–Tropsch on iron with H$_2$/CO and H$_2$/CO$_2$ as synthesis gases: the episodes of formation of the Fischer–Tropsch regime and construction of the catalyst, Top. Catal. 26 (2003) 41–54, https://doi.org/10.1023/-B:TOCA.0000012986.46680.28.

[46] J. Wang, Z. You, Q. Zhang, W. Deng, Y. Wang, Synthesis of lower olefins by hydrogenation of carbon dioxide over supported iron catalysts, Catal. Today 215 (2013) 186–193, https://doi.org/10.1016/j.cattod.2013.03.031.

[47] Z. Tian, C. Wang, J. Yue, X. Zhang, L. Ma, Effect of a potassium promoter on the Fischer-Tropsch synthesis of light olefins over iron carbide catalysts encapsulated in graphene-like carbon, Catal. Sci. Technol. 9 (2019) 2728–2741, https://doi.org/10.1039/c9cy00403c.

[48] K. Cheng, V.V. Ordomsky, M. Virginie, B. Legras, P.A. Chernavskii, V.O. Kazak, C. Cordier, S. Paul, Y. Wang, A.Y. Khodakov, Support effects in high temperature Fischer-Tropsch synthesis on iron catalysts, Appl. Catal. A Gen. 488 (2014) 66–77, https://doi.org/10.1016/j.apcata.2014.09.033.

[49] T. Numpilai, N. Chanlek, Y. Poo-Arporn, S. Wannapaiboon, C.K. Cheng, N. Siri-Nguan, T. Sornchamni, P. Kongkachuichay, M. Chareonpanich, G. Rupprechter, J. Limtrakul, T. Witoon, Pore size effects on physicochemical properties of Fe-Co/K-Al$_2$O$_3$ catalysts and their catalytic activity in CO$_2$ hydrogenation to light olefins, Appl. Surf. Sci. 483 (2019) 581–592, https://doi.org/10.1016/j.apsusc.2019.03.331.

[50] A.C.J. Koeken, H.M. Torres Galvis, T. Davidian, M. Ruitenbeek, K.P. de Jong, Suppression of carbon deposition in the iron-catalyzed production of lower olefins from synthesis gas, Angew. Chem. Int. Ed. 124 (2012) 7302–7305, https://doi.org/10.1002/ange.201200280.

[51] C. Zhang, G. Zhao, K. Liu, Y. Yang, H. Xiang, Y. Li, Adsorption and reaction of CO and hydrogen on iron-based Fischer-Tropsch synthesis catalysts, J. Mol. Catal. A Chem. 328 (2010) 35–43, https://doi.org/10.1016/j.molcata.2010.05.020.

[52] T. Herranz, S. Rojas, F.J. Pérez-Alonso, P. Ojeda, P. Terreros, J.L.G. Fierro, Genesis of iron carbides and their role in the synthesis of hydrocarbons from synthesis gas, J. Catal. 243 (2006) 199–211, https://doi.org/10.1016/j.jcat.2006.07.012.

[53] C. Ma, W. Zhang, Q. Chang, X. Wang, H. Wang, H. Chen, Y. Wei, C. Zhang, H. Xiang, Y. Yang, Y. Li, θ-Fe$_3$C dominated Fe@C core–shell catalysts for Fischer-Tropsch synthesis: roles of θ-Fe$_3$C and carbon shell, J. Catal. 393 (2021) 238–246, https://doi.org/10.1016/j.jcat.2020.11.033.

[54] C.G. Visconti, M. Martinelli, L. Falbo, L. Fratalocchi, L. Lietti, CO$_2$ hydrogenation to hydrocarbons over Co and Fe-based Fischer-Tropsch catalysts, Catal. Today 277 (2016) 161–170, https://doi.org/10.1016/j.cattod.2016.04.010.

[55] F. Yuan, G. Zhang, J. Zhu, F. Ding, A. Zhang, C. Song, X. Guo, Boosting light olefin selectivity in CO$_2$ hydrogenation by adding Co to Fe catalysts within close proximity, Catal. Today 371 (2021) 142–149, https://doi.org/10.1016/j.cattod.2020.07.072.

[56] K.Y. Kim, H. Lee, W.Y. Noh, J. Shin, S.J. Han, S.K. Kim, K. An, J.S. Lee, Cobalt ferrite nanoparticles to form a catalytic Co-Fe alloy carbide phase for selective CO$_2$ hydrogenation to light olefins, ACS Catal. 10 (2020) 8660–8671, https://doi.org/10.1021/acscatal.0c01417.

[57] S. Hilaire, X. Wang, T. Luo, R.J. Gorte, J. Wagner, A comparative study of water-gas-shift reaction over ceria-supported metallic catalysts, Appl. Catal. A Gen. 258 (2004) 271–276, https://doi.org/10.1016/j.apcata.2003.09.026.

[58] F.J. Pérez-Alonso, M. Ojeda, T. Herranz, S. Rojas, J.M. González-Carballo, P. Terreros, J.L.G. Fierro, Carbon dioxide hydrogenation over Fe–Ce catalysts, Catal. Commun. 9 (2008) 1945–1948.

[59] R.W. Dorner, D.R. Hardy, F.W. Williams, H.D. Willauer, Effects of ceria-doping on a CO$_2$ hydrogenation iron-manganese catalyst, Catal. Commun. 11 (2010) 816–819, https://doi.org/-10.1016/j.catcom.2010.02.024.

[60] C. Nie, H. Zhang, H. Ma, W. Qian, Q. Sun, W. Ying, Effects of Ce addition on Fe–Cu catalyst for Fischer–Tropsch synthesis, Catal. Lett. 149 (2019) 1375–1382, https://doi.org/-10.1007/s10562-019-02700-2.

[61] X. Wang, J. Zhang, J. Chen, Q. Ma, S. Fan, T. sheng Zhao, Effect of preparation methods on the structure and catalytic performance of Fe-Zn/K catalysts for CO$_2$ hydrogenation to light olefins, Chin. J. Chem. Eng. 26 (2018) 761–767, https://doi.org/10.1016/j.cjche.2017.10.013.